Journal of Alloys and Compounds 509 (2011) 2044–2049

Contents lists available at ScienceDirect

Journal of Alloys and Compounds

journal homepage: www.elsevier.com/locate/jallcom

Monoclinic α-Bi_2O_3 photocatalyst for efficient removal of gaseous NO and HCHO under visible light irradiation

Zhihui Ai[a,b,*], Yu Huang[b], Shuncheng Lee[b,**], Lizhi Zhang[a]

[a] Key Laboratory of Pesticide & Chemical Biology of Ministry of Education of College of Chemistry, Central China Normal University, Wuhan 430079, People's Republic of China
[b] Department of Civil and Structural Engineering, Research Center for Environmental Technology and Management, The Hong Kong Polytechnic University, Hong Kong, People's Republic of China

ARTICLE INFO

Article history:
Received 29 June 2010
Received in revised form 22 October 2010
Accepted 22 October 2010
Available online 4 November 2010

Keywords:
α-Bi_2O_3
$(BiO)_2CO_3$
Visible-light
Photocatalysis

ABSTRACT

The investigation was focused on the visible-light-driven photocatalytic removal of gaseous NO and HCHO at typical indoor air concentration over synthetic α-Bi_2O_3. Monoclinic α-Bi_2O_3 was synthesized via calcination of hydrothermally prepared $(BiO)_2CO_3$ precursor at 500 °C for 4 h. The synthetic α-Bi_2O_3 samples were systematically characterized by XRD, SEM, FT-IR, and UV–vis diffuse reflectance spectra (DRS). The optical band gap energy of the resulting α-Bi_2O_3 was estimated to be 2.72 eV from the UV–vis absorption spectra. Comparing with the commercial Bi_2O_3 counterpart, the fabricated α-Bi_2O_3 showed superior visible-light-induced photocatalytic activity on degradation of nitrogen monoxide (NO) and formaldehyde (HCHO) at typical indoor air concentration. No obvious deactivation of synthetic α-Bi_2O_3 was observed during the prolonged photocatalytic reaction. This work suggests that the synthesized monoclinic α-Bi_2O_3 with suitable band gap and high activity is promising photocatalyst for indoor air purification.

© 2010 Elsevier B.V. All rights reserved.

1. Introduction

Recently, indoor air quality (IAQ) within buildings has been paid more and more attention with increasing awareness of the public environment and health, especially in urban cities [1,2]. Indoor air pollutants mainly include carbonyl compounds, nitrogen oxides (NO_x) and volatile organic compounds (VOCs), which can cause adverse health impacts on occupants [3]. Formaldehyde (HCHO) is the representative omnipresent indoor air pollutants coming from the furnishings and decorating materials. In China, the concentration of indoor formaldehyde usually might be at ppbv to ppmv levels, which is much higher than that of the WHO guideline (80 ppbv, or 0.1 mg m^{-3}) [4–6]. Hence, it is still a challenge to develop simple and cost-effective technologies for indoor air pollutants purification.

A number of techniques, including physical adsorption, biofiltration, thermal catalysis, and photocatalytic oxidation, have been well-established for purification of indoor air pollutants. Among them, photocatalysis technology is most widely used for the purification of a wide range of indoor air contaminants [3,7–9]. For instance, TiO_2 immobilized on different substrates, such as activate carbon and glass fibers, can photocatalytically degrade indoor air pollutants in a flow system under UV light irradiation [3,10–12]. However, the widely used TiO_2 is only active in the UV range due to its relatively wide band gap (3.2 eV), which occupies no more than 4% of the solar spectrum. Although dye-sensitized and transition metal-doped or nonmetal-doped TiO_2 makes the utilization of visible light possible, many researchers focus their efforts on the development of novel non-TiO_2 catalysts with low band gaps [15–19]. This interest is due to the fact that stable and efficient dyes are usually rare, whereas dopants are inevitably a recombination centers for the photogenerated electrons and holes. Though some researchers are working on other methods to make it practical, such efforts have not yet achieved satisfactory results. Recently, some narrow band gap non-TiO_2 metal oxide semiconductors, such as $CdBiO_2Cl$ [20], $BiVO_4$ [21], $LaNiO_3$ [22], Cd_2SnO_4 [23], $InNbO_4$ [24], and BiOBr [25] have been applied in the photodegradation of organic pollutants under visible light irradiation. All these photocatalysts contain a central metal ion with d^{10} or d^0 electronic configuration, which has been reported to be favorable for the separation of photogenerated electron/hole pairs.

Bismuth oxide (Bi_2O_3) with four main crystallographic polymorphs denoted by α-, β-, γ-, and δ-Bi_2O_3 is a *p*-type semiconductors. Bi_2O_3 has been widely used in a variety of areas, such as sensor technology, optical coatings and elec-

* Corresponding author at: Key Laboratory of Pesticide & Chemical Biology of Ministry of Education of College of Chemistry, Central China Normal University, 152 Luoyu Road, Wuchang, Wuhan 430079, People's Republic of China.
Tel.: +86 27 6786 7535; fax: +86 27 6786 7535.
** Corresponding author. Tel.: +852 2766 6011; fax: +852 2766 6011.
E-mail addresses: jennifer.ai@mail.ccnu.edu.cn (Z. Ai), ceslee@polyu.edu.hk (S. Lee).

0925-8388/$ – see front matter © 2010 Elsevier B.V. All rights reserved.
doi:10.1016/j.jallcom.2010.10.132

trochromic materials due to its high refractive index, dielectric permittivity, marked photoconductivity, as well as photoluminescence (PL) [26–36]. Furthermore, it has attracted extensively interests for water decomposition and organic photocatalytic degradation under visible light illumination due to its narrow band gap about 2.8 eV [28–31]. Many methods have been developed to prepare different Bi_2O_3 structures, such as hierarchical nanostructures, nanowires, sub-micrometer rods, rippled Bi_2O_3 nanobelts, mesoporous films, and so on [26–29,33,36]. For example, Eberl and his coworker reported that Bi_2O_3 prepared after thermal decomposition of commercial $(BiO)_2CO_3$ at 500 °C showed a moderated visible-light photocatalytic activity on degradation of 4-chlorophenol in aqueous solution [31]. Ma's group synthesized Bi_2O_3 microspheres with nanopore structure through thermal decomposition of the precursor at 400 °C for 3 h in air, which was prepared using $Bi(NO_3)_3{\cdot}5H_2O$ and poly(vinylpyrrolidone) (PVP) by a microwave-assisted heating method in ethylene glycol (EG) at 150 °C for 10 min [34]. Liu et al. prepared a series of Bi_2O_3–TiO_2 composite photocatalysts with a nonaqueous sol–gel method [35]. Nanocrystalline Bi_2O_3 was prepared by sonochemical method and applied for photodegradation of methyl orange with visible light ($\lambda > 400$ nm), but this method requires a surfactant and high energy ultrasound irradiation [37]. Bi_2O_3 nanoplates were fabricated directly from commercial bulk bismuth oxide crystals by hydrothermal treatment [38]. As the photocatalytic activity of photocatalysts closely interrelates with their size, morphology, and microstructures, therefore, it is highly desirable to fabricate Bi_2O_3 with high activity that are cost-effective and allow large-scale production from the practical point of view.

Herein, for the first time we reported a hydrothermal preparation subsequent calcination route to the monoclinic α-Bi_2O_3 catalysts and their visible light photocatalytic degradation of NO and HCHO at typical concentrations for indoor air quality. HCHO was selected as a model indoor air pollutant for two reasons: it is a compound for which photocatalytic oxidation pathways have been studied extensively, and it is one of the predominant VOCs in indoor environments. The synthetic α-Bi_2O_3 catalyst exhibited higher photocatalytic activity over commercial Bi_2O_3 counterparts and showed high photochemical stability in the oxidation of NO in gas phase under visible light irradiation. This research provides a potential energy-saving technique for indoor air purification.

2. Experimental

2.1. Synthesis

All chemicals in this study were of commercially available analytical grade. Deionized water was used in all experiments. The synthetic monoclinic α-Bi_2O_3 photocatalyst was synthesized via hydrothermal method followed by calcinations. In a typical procedure, 5 mmol of $Bi(NO_3)_3{\cdot}5H_2O$ and 20 mmol of $CO(NH_2)_2$ were dissolved into 35 mL of deionized water to form two transparent solutions, respectively. The two solutions were mixed together and agitated vigorously for 10 min, then transferred to a 100 mL Teflon-lined stainless steel autoclave and heated at 160 °C for 12 h. After the autoclave was cooled naturally to room temperature, the white $(BiO)_2CO_3$ precursor precipitates were filtered and washed repeatedly with deionized water and absolute alcohol and dried at 60 °C. At last the $(BiO)_2CO_3$ precursor powder was calcined in a boat crucible at 500 °C for 4 h under air to obtain a yellow Bi_2O_3 powder.

2.2. Characterizations

X-ray powder diffraction patterns were obtained on a Bruker D8 Advance X-ray diffractometer with Cu Kα radiation ($\lambda = 1.54178$ Å). Scanning electron microscopy images were performed on a LEO 1450VP scanning electron microscope. Thermal analysis was determined on TG–DSC analysis at a heating rate of 10 °C/min under the air. UV–vis diffuse reflectance spectra were recorded at room temperature with the Cary 300 UV–visible spectrophotometer equipped with an integrated sphere. FT-IR spectra were recorded on a Nicolet Nexus spectrometer with the standard KBr pellet method. The nitrogen adsorption and desorption isotherms at 77 K were measured using a Micromeritics ASAP2010 system after samples were vacuum-dried at 473 K overnight.

2.3. Photocatalytic experiments

The photocatalytic activity experiments for degradation of NO and HCHO at typical concentrations for indoor air quality were performed at ambient temperature in a continuous flow reactor. The volume of the rectangular reactor which was made of stainless steel and covered with Saint-Glass was 4.5 L (10 cm × 30 cm × 15 cm ($H \times L \times W$)). One dish containing the 0.2 g of photocatalyst powders was placed in the middle of the reactor. A 300 W commercial tungsten halogen lamp (General Electric) was used as the light source. The lamp was vertically placed outside the reactor above the sample dish and a glass filter was placed to remove light below 420 nm. Four mini-fans were fixed around the lamp to avoid the temperature rise of the flow system. The integrated UV intensity in the range 310–400 nm was 720 ± 10 μW/cm^2. The photocatalyst samples were prepared by coating an aqueous suspension of the resulting samples onto a dish with a diameter of 12 cm. The dishes containing the photocatalyst were pretreated at 70 °C until complete removal of water in the suspension and then cooled to room temperature. NO and HCHO gas were selected as the target pollutant for the photocatalytic degradation at ambient temperature. The NO gas was acquired from a compressed gas cylinder at a concentration of 48 ppm NO (N_2 balance, BOC gas) with traceable National Institute of Stands and Technology (NIST) standard. The HCHO gas was obtained from Linde Canada Limited at a concentration of 100 ppm. The initial concentration of NO and HCHO were diluted to about 400 ppb and 2 ppm by the air stream supplied by a zero air generator (Thermo Environmental Inc. model 111), respectively. The desired humidity level of the NO and HCHO flow was controlled at 70% (2100 ppmv) by passing the zero air streams through a humidification chamber. The gas streams were premixed completely by a gas blender, and the flow rate was controlled at 4 L/min by a mass flow controller. After the adsorption–desorption equilibrium among water vapor, gases, and photocatalysts was achieved, the lamp was turned on. The concentration of NO was continuously measured by a chemiluminescence NO analyzer (Thermo Environmental Instruments Inc. model 42c), which monitors NO and NO_2 with a sampling rate of 0.7 L/min. The removal rate (%) of NO was the ratio of the concentration of NO_x (NO and NO_2) remaining in the reactor and the concentration of NO in the feeding stream. The reaction of NO with air was ignorable when performing a control experiment with or without light in the absence of photocatalyst.

As per the HCHO analysis, firstly, an acidified 2,4-dintrophenylhydrazine (Waters Sep-Pak DNPH-silica) equipped with a Desert Research Institute (DRI)'s standard carbonyl sampler was used to collect the HCHO according to the USEPA TO-11 method. After sampling, all the cartridges were capped and wrapped in pouches provided by Waters. The pouches were stored in a refrigerator at −10 °C and were analyzed within one week. The cartridge was then eluted with 5 mL of acetonitrile (HPLC grade). At last, the DNPH-carbonyl derivatives were analyzed by injecting 20 μL of the sample into a high performance liquid chromatography (HPLC, Perkin Elmer Series 200). The HPLC system consisted of a dual wavelength absorbance detector (Perkin Elmer UV/vis) operating at 365 nm with a binary pump (Perkin Elmer Series 200) and an in-line degasser. A nova-Pak (Waters) C18 reverse phase column (150 mm × 3.9 mm) with a particle size of 4 mm and pore size of 60 Å was used to separate the hydrazones. The use of the reverse phase column is to facilitate the separation of HCHO from other aliphatic hydrazones since the hydrazones are eluted in the order of decreasing polarity. The mobile phase consisted of two solvent mixtures, namely mixture A: 6:3:1 (v/v) of water/acetonitrile/tetrahydrofuran; and mixture B: 4:6 (v/v) of water/acetonitrile. The gradient program is 100% A for 1 min, followed by a linear gradient from 100% A to 100% B in 10 min. The flow rate is 1.5 mL/min. The HCHO concentration was calibrated by a standard purchased from Superco (CARB Method 1004 DNPH Mix 2). The removal rate (%) of HCHO was the ratio of the concentration of HCHO in the feeding stream and the concentration of HCHO in the outlet stream. For comparison, the similar photodegradation experiment using commercial Bi_2O_3 counterparts (Sigma) was also carried out. The schematic diagram of the experimental setup is shown in Fig. 1.

3. Results and discussion

3.1. XRD patterns of the as-prepared samples

The powder X-ray diffraction (XRD) pattern provides crystallinity and phase structures information for the samples obtained by hydrothermal method and calcinations (Fig. 2). As seen from curve a in Fig. 2, the hydrothermally synthesized white precursor could be indexed to a pure tetragonal phase of bismutite ($(BiO)_2CO_3$) (JCPDS file No. 41-1488). Accordingly, decomposition of $(BiO)_2CO_3$ precursor at 500 °C for 4 h led to slightly yellow powder. The diffraction peaks in the XRD pattern of these yellow powders can be indexed to monoclinic α-Bi_2O_3 according to the standard XRD data file (JCPDS file No. 71-2274), belonging to space group $P21/c$, which lattice constants were: $a = 5.850$ Å, $b = 8.170$ Å, $c = 7.512$ Å (curve b in Fig. 2). No other impurity phases were found, indicating the good phase purity of the products. Therefore, the

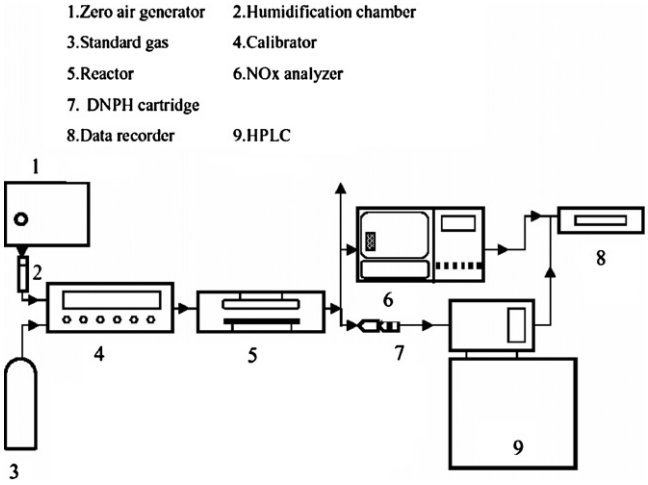

Fig. 1. Schematic diagram of the experimental setup.

monoclinic α-Bi_2O_3 have been successfully synthesized through calcinations of $(BiO)_2CO_3$ precursor at 500 °C for 4 h.

3.2. Thermal analysis of the $(BiO)_2CO_3$ precursor

The thermal decomposition behavior of the $(BiO)_2CO_3$ precursor was studied using thermogravimetric-differential scanning calorimetry (TG–DSC). As shown in Fig. 3, only one step weight loss of ca. 10.8% is observed ranging from 100 to 800 °C for the $(BiO)_2CO_3$ precursor from the TG curve, which is close to the calculated loss due to the removal of CO_2 (theoretical weight loss is 10.7%), indicating the decomposition of $(BiO)_2CO_3$ to form α-Bi_2O_3 and CO_2 in this stage. As per the DSC curve, there are two main endothermic peaks nearby 398 °C and 748 °C as well as two exothermic peaks around 288 °C and 620 °C, suggesting four evident phase transition processes. Usually, β-Bi_2O_3 can transform to α-Bi_2O_3 at about 300 °C, at around 730 °C the transition of monoclinic α-Bi_2O_3 into the δ phase occurs, cooling δ-Bi_2O_3 to a temperature of about 630 °C leads to γ-Bi_2O_3 [31]. Therefore, in our case, the endothermic peaks at 398 °C and 748 °C can be ascribed to the phase formation of α-Bi_2O_3 and δ-Bi_2O_3, respectively, while the exothermic peak around 288 °C may be ascribed to the formation of β phase Bi_2O_3, the other exothermic peak around 620 °C might be attributed to the transformation from δ-Bi_2O_3 to γ-Bi_2O_3. According to this, we could

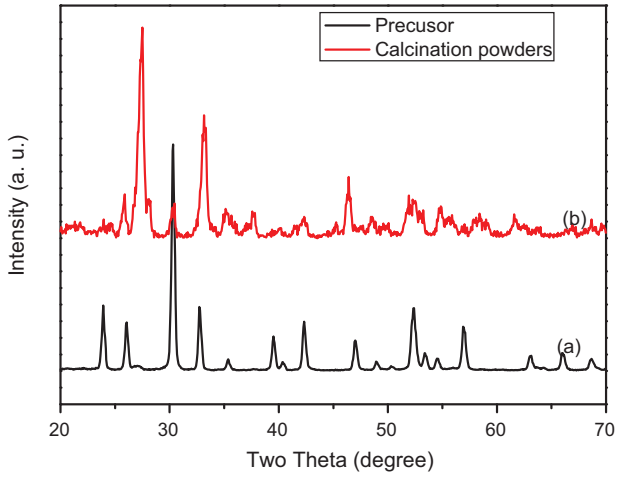

Fig. 2. XRD patterns of the precursor (black curve, a), the calcinations powders (red curve, b). (For interpretation of the references to color in this figure legend, the reader is referred to the web version of the article.)

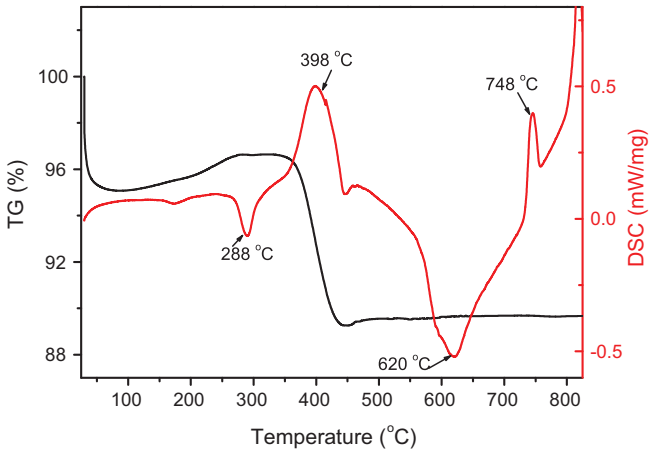

Fig. 3. TG–DSC curves of the $(BiO)_2CO_3$ precursor.

conclude that the precursor completely decomposed above 300 °C in one step to form Bi_2O_3. These results are in good agreement with the literatures' reports [29,31].

3.3. SEM images of the as-prepared samples

The morphology of the resulting samples was investigated by scanning electron microscopy (SEM). As shown in Fig. 4, we found that the obtained $(BiO)_2CO_3$ precursor was plate-like as it consisted plenty of well-defined plates with a side length of 0.5–2 μm and a thickness of about 100 nm with about 100% ratio (Fig. 4a). Never-

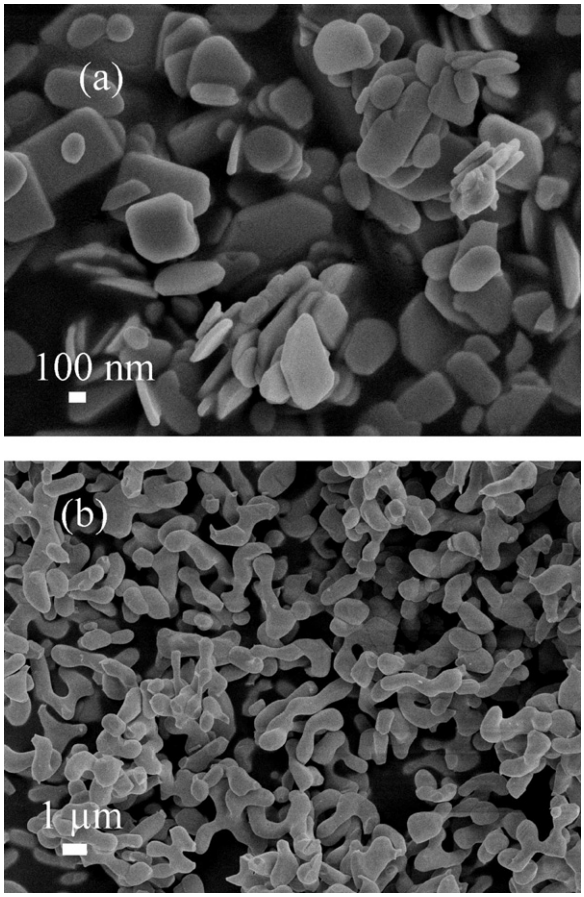

Fig. 4. SEM images of the $(BiO)_2CO_3$ precursor (a) and the prepared monoclinic α-Bi_2O_3 powders (b).

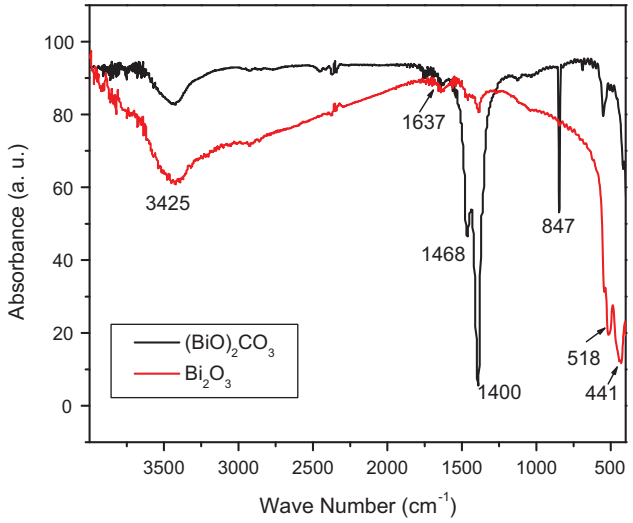

Fig. 5. FT-IR spectra of the $(BiO)_2CO_3$ precursor (black curve) and the prepared monoclinic α-Bi_2O_3 powders (red curve). (For interpretation of the references to color in this figure legend, the reader is referred to the web version of the article.)

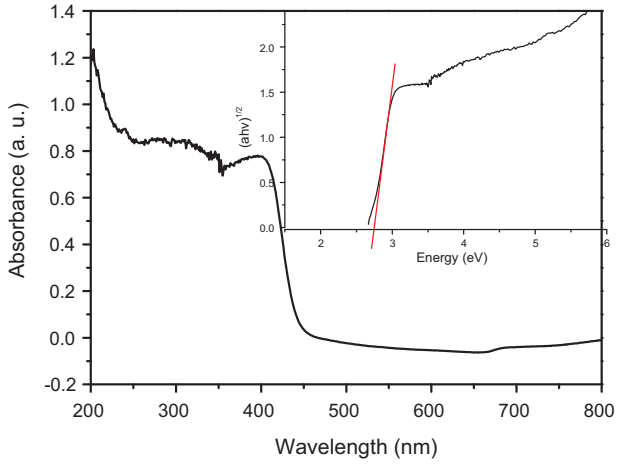

Fig. 6. The absorption spectra of the prepared monoclinic α-Bi_2O_3 samples between 200 and 800 nm. Inset shows their diffuse reflectance absorption spectra, data are plotted as transformed Kubelka–Munk function vs the energy of light.

theless, the plate-like morphology of the precursor would not be remained after calcinations. It can be seen that the resulting monoclinic α-Bi_2O_3 catalysts have irregular peanut-like shapes, which are 2–5 μm in length and about 1 μm in width (Fig. 4b).

3.4. FI-IR spectra of the as-prepared samples

The obtained $(BiO)_2CO_3$ precursor and monoclinic α-Bi_2O_3 catalysts were further characterized by FT-IR spectra to identify the functional groups on their surface (Fig. 5). The broad band at 3425 cm^{-1} is believed to be associated with the stretching vibrations of hydrogen-bonded surface water molecules and hydroxyl groups. The band at 1637 cm^{-1} corresponds to the existence of residual hydroxyl groups, which implies the O–H vibrating mode of traces of adsorbed water. Additionally, the bands located at 1468 and 1400 cm^{-1} are assigned to the C=O group vibrations in $(BiO)_2CO_3$ precursor. Comparing with two spectra, we found that the characteristic peaks of the C=O disappeared after the calcinations, indicating that the CO_2 molecules could be removed completely from $(BiO)_2CO_3$ precursor at 500 °C. The additional peaks located at 518 and 441 cm^{-1} are ascribed to be the vibration of Bi–O bonds of BiO_6 coordination polyhedra in both the $(BiO)_2CO_3$ precursor and the α-Bi_2O_3 catalysts. It needs to mention that the absorption band at about 847 cm^{-1} observed in the precursor was also disappeared in the spectrum of Bi_2O_3 catalysts, indicating the vibrations of Bi–O caused by the interaction between the Bi–O bonds and their C–O surroundings was also cleared away after the calcinations. The FT-IR analysis presented here is consistent with the results reported in the literatures [29].

3.5. UV–vis DRS spectra of the as-prepared α-Bi_2O_3 catalysts

We studied the optical absorption of the as-prepared α-Bi_2O_3 catalyst to estimate its energy band gaps. As presented in Fig. 6, the UV–vis spectra of the resulting α-Bi_2O_3 catalyst present the photoabsorption properties from UV light region to visible light shorter than 470 nm, which is assigned to the intrinsic band gap absorption. The steep shape of the spectra indicated that the light absorption was due to the band gap transition. This permits the as-prepared α-Bi_2O_3 catalyst to respond to a wide range of solar spectrum and utilize visible light for photocatalysis. The absorption band gap energy, E_g, can be determined by the Kubelka–Munk function: $(\alpha h\upsilon)^n = K(h\upsilon - E_g)$, where $h\upsilon$ is the photoenergy, α is the absorption coefficient, K is a constant relative to the material, n decides the characteristics of the transition in a semiconductor. In our experiment, assuming the material to be indirect semiconductors, like TiO_2, the energy band gaps of the synthetic α-Bi_2O_3 could be estimated from the tangent line in the plot of the square root of Kubelka–Munk functions against photon energy (inset of Fig. 6). The tangent line, which is extrapolated to $(\alpha h\upsilon)^{1/2} = 0$, indicates the band gaps of the Bi_2O_3 is 2.72 eV. This value was a little smaller than the reported value (2.85 eV) [31].

3.6. Photocatalytic degradation of NO and HCHO

The resulting monoclinic α-Bi_2O_3 catalysts were used to photocatalytically degrade NO and HCHO in order to demonstrate their potential indoor air purification application (Fig. 7). Fig. 7a shows the variation of NO concentration (C/C_0) with irradiation time over the obtained monoclinic α-Bi_2O_3. Here, C_0 is the initial concentration of NO, and C is the concentration of NO_x after photocatalytic degradation for time t. As a comparison, direct photolysis of NO, and photocatalytic oxidation of NO on commercial Bi_2O_3 counterpart were also performed under identical conditions. As shown in Fig. 7a, NO photocatalysis without the photocatalyst can almost be neglected. The photodegradation of NO on the commercial Bi_2O_3 counterpart was only 24.4%. Interestingly, the synthetic α-Bi_2O_3 showed higher photocatalytic activity under visible light and their NO removal rates reached 35.2%. The NO removal efficiency of the synthetic α-Bi_2O_3 was also much higher than Degussa TiO_2 P25, which could only remove 8% NO in 10 min under UV–visible light irradiation [3,25]. For a clearly quantitative comparison, we used the Langmuir–Hinshelwood model (L–H) to describe the rates of photocatalytic oxidation of NO on synthetic α-Bi_2O_3 [39]. The initial photocatalytic degradation of NO was found to follow mass-transfer-controlled first-order kinetics approximately as a result of low concentration target pollutants, as evidenced by the linear plot of $\ln(C/C_0)$ versus photocatalytic reaction time t. The initial rate constants of the NO degradation over the synthetic α-Bi_2O_3 under visible light irradiation were estimated to be 0.0549 min^{-1}. These constants are significantly higher than that (0.0483 min^{-1}) over the commercial Bi_2O_3 counterpart (Fig. 7b). In other words, the visible light photocatalytic activity of the synthetic α-Bi_2O_3 is higher than that of commercial Bi_2O_3.

The photocatalytic oxidation of gaseous NO has been proposed to involve reactions displayed in Eqs. (1)–(4), in which nitrogen

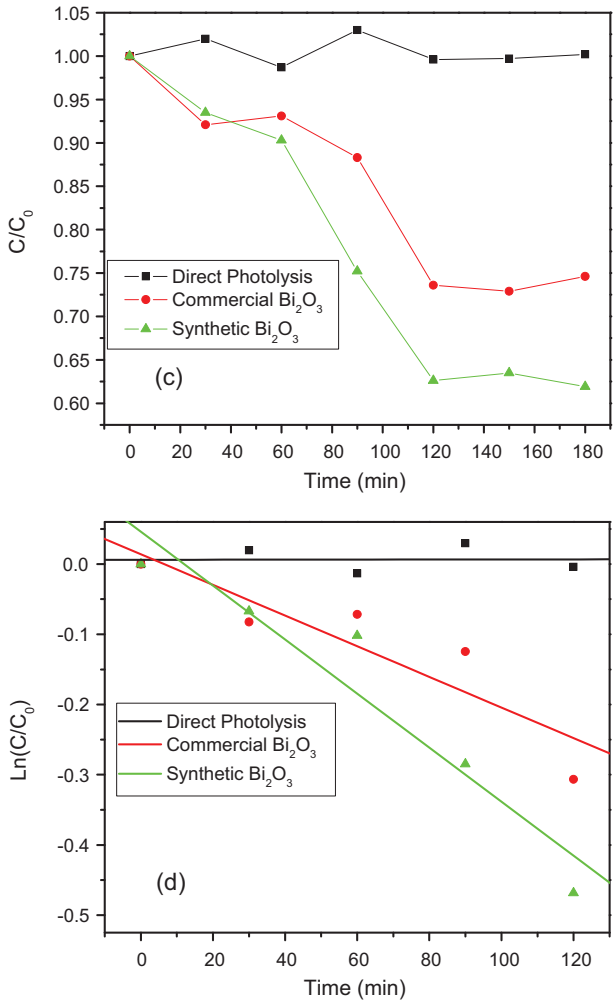

Fig. 7. Plots of the decrease in the concentrations of NO_x (a) and HCHO (c) vs irradiation time in the presence of synthetic α-Bi_2O_3 catalysts, commercial Bi_2O_3 counterpart, and direct photolysis; dependence of $\ln(C/C_0)$ on irradiation time in the presence of synthetic α-Bi_2O_3 catalysts, commercial Bi_2O_3 counterpart under visible-light irradiation (λ > 420 nm), NO (b) and HCHO (d).

monoxide reacts with reactive radicals to produce HNO_2 and HNO_3 [25].

$$NO + 2{}^{\bullet}OH \rightarrow NO_2 + H_2O \quad (1)$$

$$NO_2 + {}^{\bullet}OH \rightarrow NO_3{}^- + H^+ \quad (2)$$

$$NO + NO_2 + H_2O \rightarrow 2HNO_2 \quad (3)$$

$$NO_x + {}^{\bullet}O_2{}^- \rightarrow NO_3{}^- \quad (4)$$

In the present study, the inlet HCHO concentration was conditioned to 2 ppm, which is the common level in "sick buildings". The typical plots describing the decrease in the concentration of HCHO as a function of reaction time are shown in Fig. 7c. Similarly, HCHO would not be photolyzed under visible light irradiation (λ > 420 nm). The photodegradation of HCHO on the commercial Bi_2O_3 was only 26.4%, whereas the synthetic α-Bi_2O_3 showed higher photocatalytic activity as their HCHO removal rates reached 37.4%. Similarly, we also calculated the initial rate constants of the synthetic α-Bi_2O_3 and the commercial Bi_2O_3 counterpart for the degradation of HCHO (Fig. 7d). The initial rate constant of the HCHO degradation over the synthetic α-Bi_2O_3 under visible light irradiation was estimated to be 0.00385 min^{-1}. This constant is significantly higher than that (0.00218 min^{-1}) over the commercial Bi_2O_3 counterpart, revealing the superior photocatalytic activity of synthesized α-Bi_2O_3 under visible light.

The photocatalytic oxidation of gaseous formaldehyde has been proposed to involve a carbonyl-radical-mediated chain reaction, which is mediated by hydroxyl radicals, superoxide radicals, and/or hydrogen peroxide. These active species result from the trapping of photogenerated electrons by oxygen of the trapping of photogenerated holes by H_2O and hydrated surface of catalysts. Under a specific illumination, if the number of HCHO molecules adsorbed on Bi_2O_3 surface is much larger than the number of photogenerated holes on the Bi_2O_3 surface, most of the absorbed HCHO molecules will be oxidized to formic acid (Eq. (5)) [4–6]. When the number of the holes photogenerated on Bi_2O_3 surface is much larger than the number of the adsorbed HCHO molecules, the proportion of mineralization of HCHO to CO_2 might increase (Eq. (6)) [40].

$$HCHO + H_2O + h^+ \rightarrow HCOOH + H^+ \quad (5)$$

$$HCHO + H_2O + h^+ \rightarrow CO_2 + H^+ \quad (6)$$

Generally, the overall photocatalytic activity of a semiconductor is primarily decided by its specific surface area, structure, morphology, photoabsorption ability in the available light energy region, and electronic configuration. The specific surface area of the synthetic α-Bi_2O_3 calculated by the BET method was 6.23 $m^2\,g^{-1}$, which is almost same as that of the commercial Bi_2O_3 (6.16 $m^2\,g^{-1}$). In addition, the crystalline structure of the commercial Bi_2O_3 is also monoclinic α. Therefore, the high photocatalytic activity of the synthetic α-Bi_2O_3 could not be attributed to its large specific surface area and structure. The effective activity of the synthetic α-Bi_2O_3 photocatalyst should be attributed to their morphology, visible-light response and special electronic configuration. It is well-known that the high diffuse absorption coefficient of a catalyst causes strong light absorption, which is desirable for the enhancement of activity. The peanut-shaped Bi_2O_3 possessed a high photoabsorption coefficient in the visible light region and a narrow band gap (2.72 eV) (see Fig. 6), indicating that the as-prepared monoclinic α-Bi_2O_3 can utilize visible light effectively. Additionally, the intrinsic polarizabilities induced by Bi 6s2 lone electron pairs in the monoclinic α-Bi_2O_3 are favorable for the separation of photogenerated electron–hole pairs and the transfer of these charge carriers, as well as their wide delocalized bands is beneficial to the diffusion of photogenerated charge carriers [41].

3.7. *Stability of the synthetic α-Bi_2O_3 photocatalysts*

The stability of a photocatalyst is important for its practical application. Comparing with aqueous-phase photocatalytic reaction, an important disadvantage existing in gas-phase photocatalytic reactions is that the intermediates generated by photocatalysis would accumulate on the surface of the photocatalyst to deactivate the photocatalyst during the photocatalytic process in the gas phase, while water is able to remove reaction intermediates from the photocatalyst surface in aqueous-phase photocatalytic reaction system, which can alleviate the deactivation of photocatalyst [39,42]. It was reported that the N-doped TiO_2 and sulfide photocatalysts sometimes suffer from instability under repeated use [25]. To further study the stability of the synthetic α-Bi_2O_3 photocatalysts on photocatalytic oxidation of NO in gas phase, we carried out multiple runs of photocatalytic experiment with the used synthetic α-Bi_2O_3 photocatalysts (Fig. 8a). It was interesting to find that the synthetic α-Bi_2O_3 photocatalysts were chemically stable after eight cycles of repeated experiments. Moreover, we performed a prolonged photodegradation experiment and the results of long-term catalyst stability are shown in Fig. 8b, the synthetic α-Bi_2O_3 photocatalyst was not significantly deactivated during the photodegradation, suggesting that

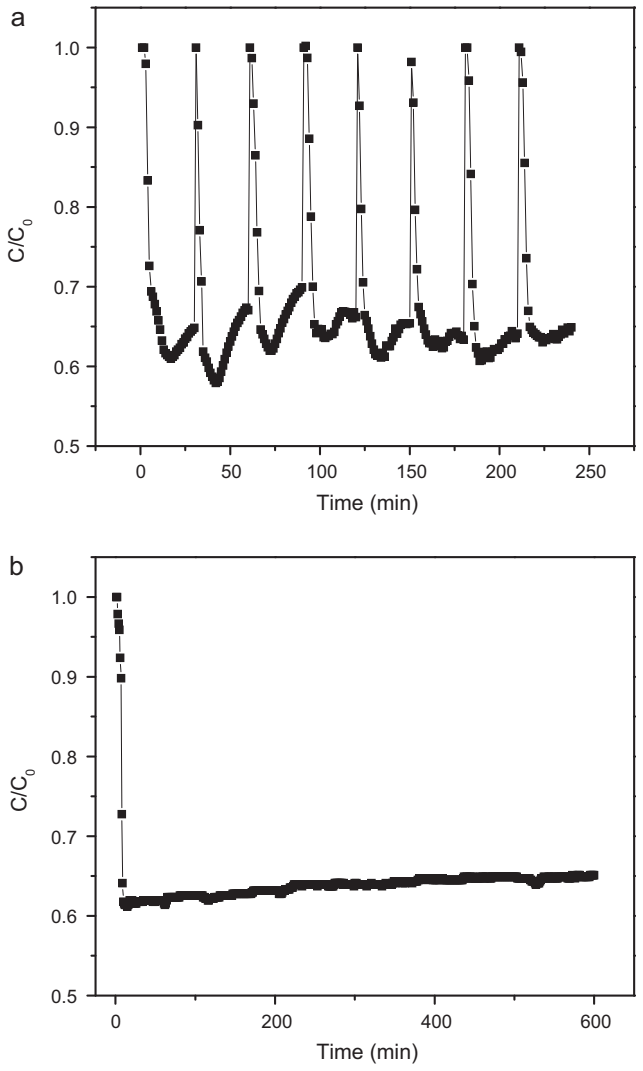

Fig. 8. (a) The stability of synthetic monoclinic α-Bi_2O_3 catalysts in multiple runs of degradation of NO; (b) the plots of the decrease in NO concentration vs prolonged irradiation time.

the as-prepared α-Bi_2O_3 photocatalysts are promising candidate for indoor air purification under visible light irradiation.

4. Conclusions

In summary, we prepared monoclinic α-Bi_2O_3 with high efficient visible-light-driven photocatalytic activity via calcinations of hydrothermally prepared $(BiO)_2CO_3$ precursor. Photocatalytic experiments indicated that the synthetic α-Bi_2O_3 exhibited a much higher photocatalytic activity for the degradation of NO and HCHO pollutants in gas phase than that of the commercial Bi_2O_3 counterparts under visible-light irradiation. This work presents a promising approach for scaling-up industrial production of α-Bi_2O_3 photocatalysts and suggests that the synthesized α-Bi_2O_3 are promising photocatalysts for indoor air purification.

Acknowledgements

This work was supported by National Science Foundation of China (grants 20777026 and 20977039), National Basic Research Program of China (973 Program) (grant 2007CB613301), Program for Distinguished Young Scientist of Hubei Province (2009CDA014), Program for Innovation Team of Hubei Province (2009CDA048), Self-Determine Research Funds of CCNU from the Colleges' Basic Research and Operation of MOE (CCNU09A02014, CCNU09C01009), and Program for New Century Excellent Talents in University (grant NCET-07-0352), the Scientific Research Foundation for the Returned Overseas Chinese Scholars, State Education Ministry, and Open Fund of Key Laboratory of Catalysis and Materials Science of Hubei Province (CHCL09001). The work described in this paper was also partially supported by the Hong Kong Polytechnic University (GYF08, and GYX0L).

References

[1] S.L. Fischer, C.P. Koshland, Environ. Sci. Technol. 41 (2007) 3121.
[2] L.S.R. Brickus, J.N. Cardoso, F.R. de Aquino Neto, Environ. Sci. Technol. 32 (1998) 3485.
[3] Y. Huang, W.K. Ho, S.C. Lee, L.Z. Zhang, G.S. Li, J.C. Yu, Langmuir 24 (2008) 3510.
[4] C.H. Ao, S.C. Lee, Chem. Eng. Sci. 60 (2005) 103.
[5] C.H. Ao, S.C. Lee, S.C. Zou, Appl. Catal. B: Environ. 49 (2004) 187.
[6] C.H. Ao, S.C. Lee, J. Photochem. Photobiol. A: Chem. 161 (2004) 2.
[7] J.G. Yu, X.X. Yu, Environ. Sci. Technol. 42 (2008) 4902.
[8] M.A. Fox, M.T. Dulay, Chem. Rev. 93 (1993) 341.
[9] M.R. Hoffmann, S.T. Martin, W. Choi, D.W. Bahnemann, Chem. Rev. 95 (1995) 69.
[10] F.B. Li, X.Z. Li, C.H. Ao, M.F. Hou, S.C. Lee, Appl. Catal. B: Environ. 54 (2004) 275.
[11] W.K. Ho, J.C. Yu, S.C. Lee, Appl. Catal. B: Environ. 73 (2007) 135.
[12] W.K. Ho, J.C. Yu, S.C. Lee, J. Solid State Chem. 179 (2006) 1171.
[15] J.J. Xu, Y.H. Ao, M.D. Chen, D.G. Fu, J. Alloys Compd. 484 (2009) 73.
[16] D.Y. Wu, M.C. Long, W.M. Cai, C. Chen, Y.H. Wu, J. Alloys Compd. 502 (2010) 289.
[17] D. Mitoraj, H. Kisch, Angew. Chem. Int. Ed. 47 (2008) 9975.
[18] J.A. Rengifo-Herrera, E. Mielczarski, J. Mielczarski, N.C. Castillo, J. Kiwi, C. Pulgarin, Appl. Catal. B: Environ. 84 (2008) 448.
[19] W.J. Ren, Z.H. Ai, F.L. Jia, L.Z. Zhang, X.X. Fan, Z.G. Zou, Appl. Catal. B: Environ. 69 (2007) 138.
[20] F.Q. Huang, J.J. Wu, X.P. Lin, Z. Zhou, J. Alloys Compd. (2010) 081, doi:10.1016/j.jallcom.2010.09.
[21] C.Y. Chung, C.H. Lu, J. Alloys Compd. 502 (2010) L1.
[22] Y.Y. Li, S.S. Yao, W. Wen, L.H. Xue, Y.W. Yan, J. Alloys Compd. 491 (2010) 560.
[23] X.L. Huang, J. Lv, Z.S. Li, Z.G. Zou, J. Alloys Compd. 507 (2010) 341.
[24] L.Z. Zhang, I. Djerdj, M.H. Cao, M. Antonietti, M. Niederberger, Adv. Mater. 19 (2007) 2083.
[25] Z.H. Ai, W.K. Ho, S.C. Lee, Environ. Sci. Technol. 43 (2009) 4143.
[26] Y. Bessekhouad, D. Robert, J.V. Weber, Catal. Today 101 (2005) 315.
[27] H.T. Zhang, S.X. Yang, Z.S. Li, L.F. Liu, T. Yu, J.H. Ye, Z.G. Zou, J. Phys. Chem. Solids 67 (2006) 2501.
[28] J.M. Xie, X.M. Lu, M. Chen, G.Q. Zhao, Y.Z. Song, S.S. Lu, Dyes Pigm. 77 (2008) 43.
[29] L. Zhou, W.Z. Wang, H.L. Xu, S.M. Sun, M. Shang, Chem. Eur. J. 15 (2009) 1776.
[30] L.Z Li, B. Yan, J. Alloys Compd. 476 (2009) 624.
[31] J. Eberl, H. Kisch, Photochem. Photobiol. Sci. 11 (2008) 1400.
[32] L.F. Yin, J.F. Niu, Z.Y. Shen, J. Chen, Environ. Sci. Technol. 44 (2010) 5581.
[33] F.L. Zheng, G.R. Li, Y.N. Ou, Z.L. Wang, C.Y. Su, Y.X. Tong, Chem. Commun. 46 (2010) 5021.
[34] M.G. Ma, J.F. Zhu, R.C. Sun, Y.J. Zhu, Mater. Lett. 64 (2010) 1524.
[35] Y.D. Liu, F. Xin, F.M. Wang, S.X. Luo, X.H. Yin, J. Alloys Compd. 498 (2010) 179.
[36] K. Brezesinski, R. Ostermann, P. Hartmann, J. Perlich, T. Brezesinski, Chem. Mater. 22 (2010) 3079.
[37] L. Zhang, W. Wang, J. Yang, Z. Chen, W. Zhang, L. Zhou, S. Liu, Appl. Catal. A 308 (2006) 105.
[38] J.C. Yu, A.W. Xu, L.Z. Zhang, R.Q. Song, L. Wu, J. Phys. Chem. B 108 (2004) 64.
[39] Y. Ohko, Y. Nakamura, A. Fukuda, S. Matsuzawa, K. Takeuchi, J. Phys. Chem. C 112 (2008) 10502.
[40] J.L. Shie, C.H. Lee, C.S. Chiou, C.T. Chang, C.C. Chang, C.Y. Chang, J. Hazard. Mater. 155 (2008) 164.
[41] Y. Wang, Y.Y. Wen, H.M. Ding, Y.K. Shan, J. Mater. Sci. 45 (2010) 1385.
[42] S. Yin, B. Liu, P. Zhang, T. Morikawa, K.I. Yamanaka, T. Sato, J. Phys. Chem. C 112 (2008) 12425.